

Adaptive Deconvolution of Astronomical Radio Images

Lawrence Cram and Taisheng Ye

School of Physics, University of Sydney, NSW 2006, Australia.

Abstract

The novel image-forming methods used in the Molonglo Observatory Synthesis Telescope (MOST) are not amenable to a direct application of the self-calibration techniques that have been so effective in improving the performance of many other aperture synthesis radio telescopes. Specifically, self-calibration of antenna-based errors and the use of phase closure conditions is not possible because vital antenna-based information is lost irretrievably as the MOST forms interferometer beams in real time. However, it is shown in this paper that suitable *models* of errors introduced by the atmosphere and telescope can be adaptively constructed from the properties of synthesised images. These models can then be used iteratively with standard deconvolution methods to improve significantly the fidelity of MOST images. The method would have general application to tomographic imaging systems in which non-ideal behaviour could be represented by a small number of unknown parameters.

1. Introduction

Many radio telescopes are multi-element interferometers that use earth-rotation aperture synthesis to provide an imaging capability of great power. In telescopes of this kind it is usual to record the complex visibility measured by each interferometer in the array as the Earth rotates and (perhaps) as the element spacing is altered between observing sessions. An image of the radio sky can then be made by Fourier synthesis from the assembled visibilities (Christiansen and Hogbom 1985; Thompson *et al.* 1986), with an angular resolution approaching that of a filled aperture of the corresponding size.

The quality of an image formed by a synthesis telescope is frequently limited by errors introduced by propagation through the terrestrial atmosphere and/or by uncertainties in the calibration of the individual telescopes in the array. Often this limitation can be relieved and the image quality greatly improved by the application of *self-calibration* techniques, which exploit closure phase and other constraints to estimate and counteract many of the errors introduced by propagation and in the instrument (Pearson and Readhead 1984; Thompson *et al.* 1986). Dynamic ranges of the order of 100 000:1 have been obtained by the application of these techniques (e.g. Noordam and de Bruyn 1982).

Although the Molonglo Observatory Synthesis Telescope (MOST) is an earth-rotation aperture synthesis telescope, it does not record complex visibilities for each baseline in the array. Rather, the visibilities measured by the interferometers are processed in real time to yield directly the flux density distribution in

a comb of fan beams that spans the field of view. This design is used for economy (almost 8000 complex correlators would be needed to evaluate the visibilities from the highly redundant MOST) and to minimise the need for off-line computations. However, in forming the fan beams, vital information on antenna-based errors is lost irretrievably so that the conventional self-calibration methods cannot be applied to images obtained by the MOST. Fortunately, as we show in this paper, it is still possible to apply variants of the self-calibration algorithm to obtain significant improvements in the quality of images formed by the MOST.

2. Image Formation by the MOST

The majority of aperture synthesis radio telescopes record the complex fringe visibility $V(u,v)$ in the aperture plane (u,v) for each interferometer (pair of antennas) in the telescope. Following calibration and other processing stages, a radio image is formed from the visibilities by Fourier transformation (Thompson *et al.* 1986, Chapt. 10). The quality of this image may be quite poor if the telescope samples the incident electromagnetic field sparsely over the aperture plane, as is usually the case. However, powerful algorithms (Thompson *et al.* 1986, Chapt. 11) are available to interpolate and extrapolate the unmeasured visibilities, and hence to form an image that portrays more faithfully the distribution of radio brightness in the observed part of the sky.

In contrast to this procedure, the MOST does not record complex fringe visibilities for each interferometer in the telescope. Rather, the Fourier transformation that is carried out off-line in most synthesis telescopes is performed by analogue and digital electronic systems in real time in the MOST. As a consequence, the MOST records not the visibilities of the target field, but rather forms interferometer beams in real time, and records directly the flux densities detected by these beams. The imaging strategy in the MOST thus significantly reduces the burden of post-observation image processing, but at the expense of irretrievably losing information about the complex gain of individual receiving elements in the telescope.

(2a) Beam Formation

Descriptions of the operation of the MOST have been published by Mills (1981) and Robertson (1991). For our purposes, it suffices to note that the MOST comprises two linear feed lines illuminating paraboloidal reflectors (called 'arms'), each of length $2185 \cdot 8\lambda$ (MOST operates at 843 MHz, so $\lambda = 0 \cdot 356$ m) and separated by a gap of $42 \cdot 8\lambda$. The arms are horizontal and aligned in an east-west (E-W) direction. Each arm is divided into 44 contiguous, electrically independent and equally sized elements (called 'bays'). The 44 signal lines from the bays on the east arm, and the 44 signal lines from the bays on the west arm, are combined in a resistor array (Large and Frater 1969) and synchronously demodulated to produce a comb of 64 fan beam responses separated by 22 arcsec on the sky (i.e. a 23 arcmin field of view). In practice, the beams are interleaved on 2 second intervals to form 128 beams on an 11 arcsec spacing, to ensure sub-Nyquist sampling. Frequently, a field wider than the standard 23 arcmin field is observed by time-sharing the comb of beams into a total of $3 \times 128 = 384$ positions for a field size of 70 arcmin, and even wider fields are contemplated.

The natural coordinate system for the MOST is an alt-alt frame (Robertson 1991, Fig. 2) representing the separate effects of the *tilt* drive and the *meridian distance* drive. The tilt drive rotates the arms about their (long) E-W axis and the tilt direction is thus measured as the angular rotation about the E-W axis (zero in the plane containing the zenith, and positive towards the north). The meridian distance drive changes the phase/delay gradient along the arms, so that meridian distance is measured as the complement of the opening angle of the right cone whose axis coincides with the E-W line feed. For sources near meridian passage, tilt corresponds to declination while meridian distance corresponds to right ascension. The relation between the two sets of coordinates is essentially switched for sources that are rising or setting (hour angle close to -6 h or $+6$ h).

Ideally, the reception pattern (radiation pattern) of a fan beam may be regarded as the product of the *primary* reception pattern of a bay and the *interferometer* reception pattern produced by correlating the signals received by the east and west arms. The primary beam of a bay is in turn the product of the pattern in (i) the meridian distance direction and (ii) the tilt direction. The former pattern is determined by the uniform E-W grading of the bay and is thus a sinc-function. The latter is determined by the parabolic reflector mesh and receiver element pattern and has been measured to closely approximate a Gaussian. The imaging software used with the MOST does account for the primary beam, but we ignore it here since we discuss images that occupy only the inner part of the primary beam of the bays.

The interferometer beam, b , corresponding to an ideal model of the MOST, has a simple closed form,

$$b(\rho) = \text{sinc}^2(\pi L_0 \rho) \cos(2\pi[L_0 + G_0]\rho). \quad (1)$$

Here ρ is the meridian distance offset measured (in radians) from the phase centre of the fan beam, $L_0 = 2185 \cdot 8\lambda$ is the length of an arm, and $G_0 = 42 \cdot 8\lambda$ is the length of the gap. The interferometer beam extends without limit in the direction orthogonal to ρ (i.e. in the tilt direction). The function $b(\rho)$ may be understood in terms of the theory of a compound array (Bracewell 1978; Christiansen and Hogbom 1985) as follows: the first factor is a sinc-function arising from the uniform grading of an arm, and the second factor is the modulation by a cosine-function representing the spacing between the centres of the two arms. The interferometer beam shape is shown in Fig. 1.

As described above, the MOST is designed to form a comb of fan beams, each having the response described by equation (1). A normal MOST synthesis observation is made by directing the centre of the comb at the centre of the selected field, and recording the fan beam responses every 24 seconds as the sky appears to rotate about the field centre. A single 24 s observation may then be regarded as the cross-correlation of the ideal interferometer beam and the actual distribution of sky brightness, sampled at the comb spacing in the meridian distance direction, weighted by the primary beam response, and strip-integrated along the tilt direction. Fig. 1*d* shows a 24 s sample of actual data. After 12 hours have elapsed, the rotation of the Earth will have ensured that all position angles have been observed, a total of about 1792 samples having been recorded.

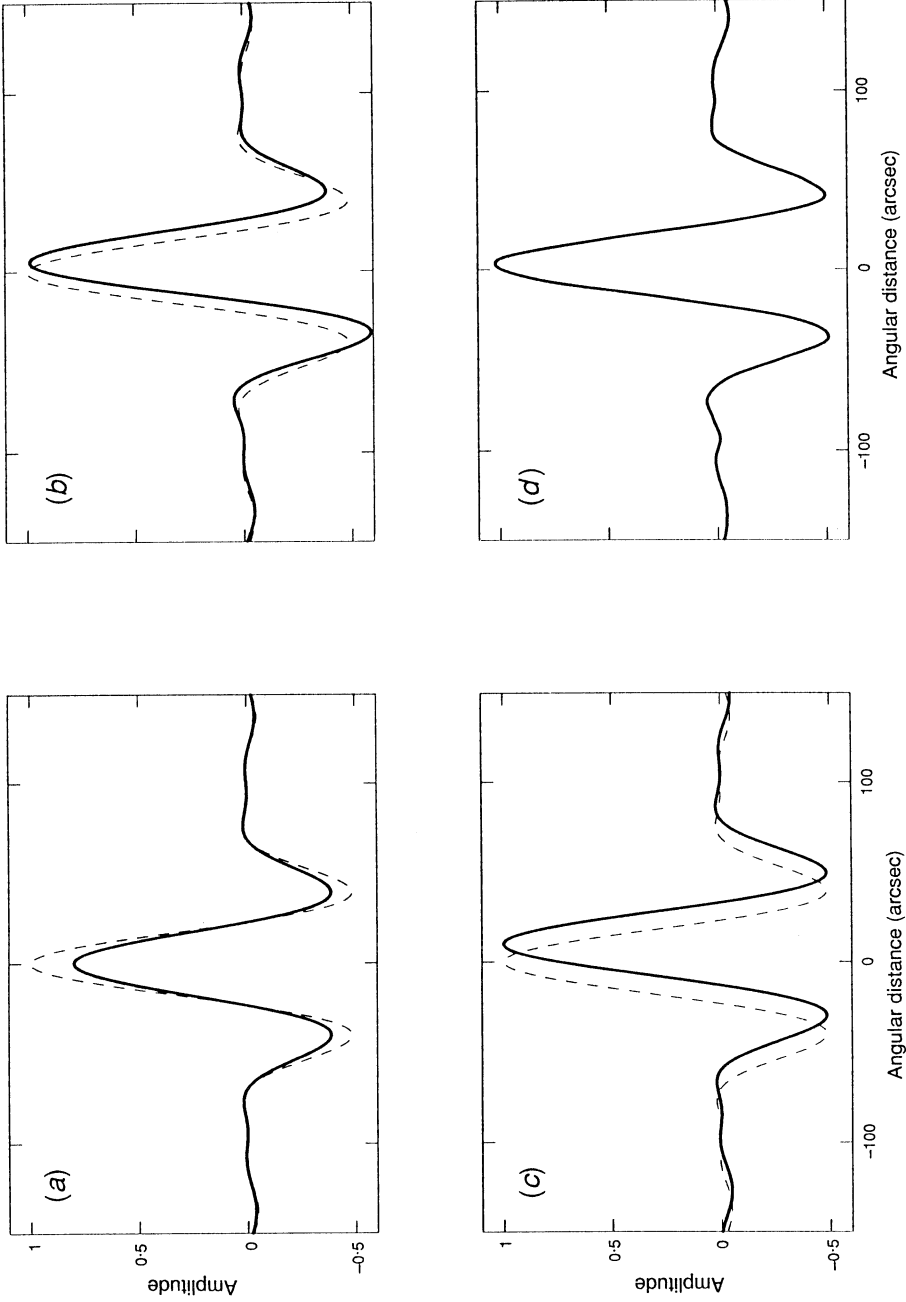


Fig. 1. The shape of the MOST interferometer beam at transit. In each frame, the ideal beam is shown as a dashed curve. The solid curves are (a) beam with $a_1 = 0.9$; (b) beam with $a_2 = 10^\circ$; (c) beam with $a_3 = 5$ arcsec; and (d) an example of actual data for a strong point source (the noise amplitude is about the thickness of the curve).

(2b) Image Formation

MOST data are assembled into a radio image using the algorithm known as 'back-projection' (Bracewell 1956, 1978; Crawford 1984). The algorithm begins with a blank image plane $B_0(\xi, \eta)$, where the coordinates (ξ, η) are defined as direction cosines relative to (u, v) . Close to the field centre, ξ and η correspond respectively to simple projections of right ascension and declination (Thompson *et al.* 1986, Chapt. 4).

A single 24 s sample, $B(\rho, H)$, measured at hour angle H , is then added into the image plane, each sample point ρ being added to all points in the image array which contributed to the original strip integral at H . These points are defined by (Perley 1979)

$$\delta(\xi \cos \theta + \eta \sin \theta - \rho) = 1, \quad (2)$$

where θ is the meridian distance (corrected for precession if desired). The next sample is added in at a slightly different value of θ corresponding to the slightly different time of observation, and so on until all samples have been added and all hour angles covered. At pixels corresponding to parts of the sky that contain positive surface brightness, the beam responses add to produce a visible object in the final image. At pixels corresponding to blank parts of the sky, equal amounts of positive and negative sidelobes of the fan beam occur and (in the ideal case) add to zero. In practice, the sum does not cancel exactly due to limited sampling and errors in the calibration—the departure from zero is used here to adaptively deconvolve the image. As the image is assembled, straightforward corrections may be made for primary beam attenuation, precession and other calibrated systematic errors.

The reconstructed image is (in principle) a convolution of the sky brightness distribution and the synthesised point spread function (PSF). The PSF is, of course, just the back projection of the one-dimensional beam shape $b(\rho)$. The CLEAN algorithm or some other deconvolution procedure (e.g. Thompson *et al.* 1986, Chap. 11) may be used to deconvolve the reconstructed image. Fig. 2a shows the outcome of back projection of a typical data set for the strong unresolved source 0409-634.

Fig. 2a reveals many artifacts, most notably radial 'spokes' emanating from the source. Such artifacts are often present in the images formed by MOST, and restrict the dynamic range to about 100:1 under normal conditions. Whilst this level is adequate for much useful astronomy, the restriction to the dynamic range is not determined by any fundamental limitation such as system noise or confusion, but rather by propagation irregularities and/or telescope errors. It would thus be possible to improve the dynamic range of MOST images if a means could be found to correct for these sources of error: such a process is now described.

3. Adaptive Deconvolution

Studies of the actual beamshape of the MOST have shown that the ideal beam given by equation (1) is usually distorted by small and characteristic deviations

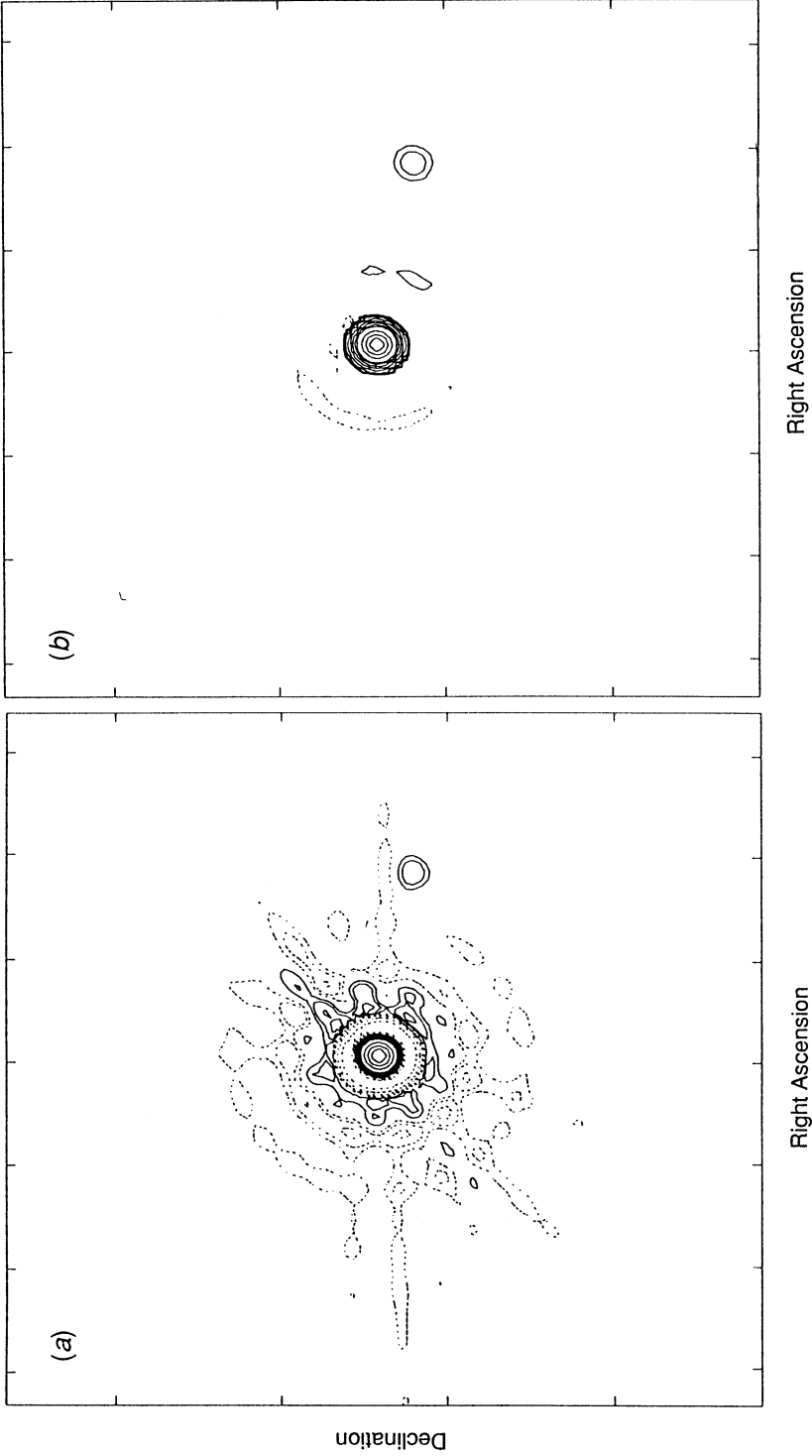


Fig. 2. Image of the strong, unresolved radio source 0409–634 made by back projection: (a) raw image, (b) adaptively deconvolved image. Note in image (a) the presence of radial artifacts and other image defects, which are made prominent here by selection of appropriate contour levels (common to both images). The weak residual artifacts in image (b) are contoured at a level of $\pm 0.4\%$ of the peak flux. The separation between two ticks is 115 arcsec in Right Ascension and 180 arcsec in Declination respectively.

that change with time. These deviations lead to a modified beam shape of the form

$$b'(\rho) = a_1 \operatorname{sinc}^2[\pi L_0(\rho - a_2)] \cos[2\pi(L_0 + G_0)(\rho - a_2) - a_3]. \quad (3)$$

Here, a_1 is a correction to the *gain* of the telescope, a_2 is a *pointing offset* in the telescope, and a_3 is a term representing the effect of a spurious step in the *phase* of the East arm relative to the West arm. Fig. 1 illustrates the characteristic patterns produced by changes in each of these parameters.

If the values of a_1 were known, the procedure outlined in Section 2 could be applied using equation (3) rather than equation (1) to generate the PSF. For many years this approach has been used when forming MOST images, with the values of a_i being estimated from observations of strong, unresolved sources (calibrators) made before and after a normal synthesis session. However, the use of a_i values determined in this way does not lead to a completely satisfactory reconstruction, because minor faults in the telescope and irregular fluctuations in the refractive properties of the atmosphere (troposphere and ionosphere) lead inevitably to small, time-dependent variations in the a_i while the synthesis is in progress. If we knew the values of $a_i(t)$ for all times t , we could correct each 24 s sample using equation (3) to produce a closer approximation to ideal behaviour. Although there is no known way to determine these time-dependent corrections by means of measurements made as the synthesis progresses, we can use the image itself to obtain iteratively a close approximation to them.

(3a) Adaptive Deconvolution Algorithm

We begin by outlining an algorithm for the adaptive deconvolution of MOST images formulated in the Fourier transform plane (Gray 1991). In general we may write (Thompson *et al.* 1986)

$$V_{\text{obs}}(u, v) = G(u, v) P_0(u, v) V_{\text{true}}(u, v) + \epsilon(u, v), \quad (4)$$

where V_{obs} and V_{true} are respectively the observed (measured) and true complex visibilities of the image, P_0 is the Fourier transform of the ideal synthesised beam, G is a complex correction factor (originally unknown) representing the difference between the ideal and actual synthesised beam, and ϵ is a zero-mean noise term. While our ultimate aim is to find V_{true} , we first want to find G . To do this, we must estimate or eliminate the unknowns V_{true} and ϵ .

We begin by approximating V_{true} by a model determined, for example, by the CLEAN algorithm (Hogbom 1974) which provides a means for identifying the positions and strengths of δ -function components of the true image. If V_{model} is the model developed in this way, the (unknown) error image V_{error} is defined as

$$V_{\text{error}} = V_{\text{true}} - V_{\text{model}}. \quad (5)$$

By substituting equation (5) into (4) we find

$$G = \left(1 + \frac{V_{\text{error}}}{V_{\text{model}}}\right)^{-1} \left(1 - \frac{\epsilon}{V_{\text{obs}}}\right) \frac{V_{\text{obs}}}{P_0 V_{\text{model}}}. \quad (6)$$

Provided that for a selected range of (u, v) we have $V_{\text{error}}(u, v) \ll V_{\text{model}}(u, v)$ and $\epsilon(u, v) \ll V_{\text{obs}}(u, v)$, it follows that

$$G(u, v) \approx \frac{V_{\text{obs}}(u, v)}{P_0(u, v) V_{\text{model}}(u, v)}. \quad (7)$$

This is an approximation to the unknown correction factor $G(u, v)$ in terms of known quantities. Note that G will have an amplitude of unity and zero phase for all (u, v) if the Fourier transform of the actual PSF, GP_0 , corresponds to the ideal PSF, P_0 . For the beam-shape model equation (3), G has the form

$$G(u, v; t) = a_1(t) \exp[i2\pi a_2(t)r + a_3(t)], \quad (8)$$

where $r = \sqrt{u^2 + v^2}$.

In conventional self-calibration the correction factor G is found by comparing the model with the measured visibilities. This is not feasible with MOST data because the primary beam of the MOST is not fully covered by the comb of beams. Thus, the recorded fan-beam responses contain many off-field sources (detected in the main beams and in the grating lobes) for which we do not have complete information. To circumvent this problem we compare the model constructed from CLEAN components in the fully synthesised part of the image with the actual image made from the raw data.

Gray (personal communication) devised an algorithm that implemented the above theory explicitly in the Fourier transform plane (u, v) . Although the approach was quite promising, Gray encountered apparently insurmountable problems in (i) the interpolation of the complex transform at arbitrary times (angles), and (ii) the treatment of zeroes in equation (8). To overcome these and other problems, we have devised an algorithm that follows the above procedure, but performs many of the required manipulations in the image plane rather than the Fourier transform plane.

We first calculate the strip integral of the model image and the observed image in each of the directions corresponding to the observing times t , by integrating the two-dimensional array along the lines defined by equation (2). This step is crucial for the success of the procedure, since it overcomes the interpolation problems in the Fourier domain. The Fourier transforms of the (one-dimensional) strip integrals are then evaluated, and the values of $a_i(t)$ are obtained by least-squares fitting to the functional form (6) over the (u, v) range where there is adequate signal-to-noise ratio. Once the a_i are estimated, the sample values may be corrected accordingly. A new image is generated by back projection of the corrected sample values and the procedure repeated until the values $a_i(t)$ do not change significantly.

(3b) Results

We have used the data leading to the image shown in Fig. 2a to test the adaptive deconvolution algorithm. Strip integration of the difference image and subsequent least-squares fitting of the amplitude and phase components of equation (8) to the region $200\lambda < r < 1000\lambda$ in the Fourier transform of the strip integral yields the values of the parameters a_i shown in Fig. 3. These values have been used to

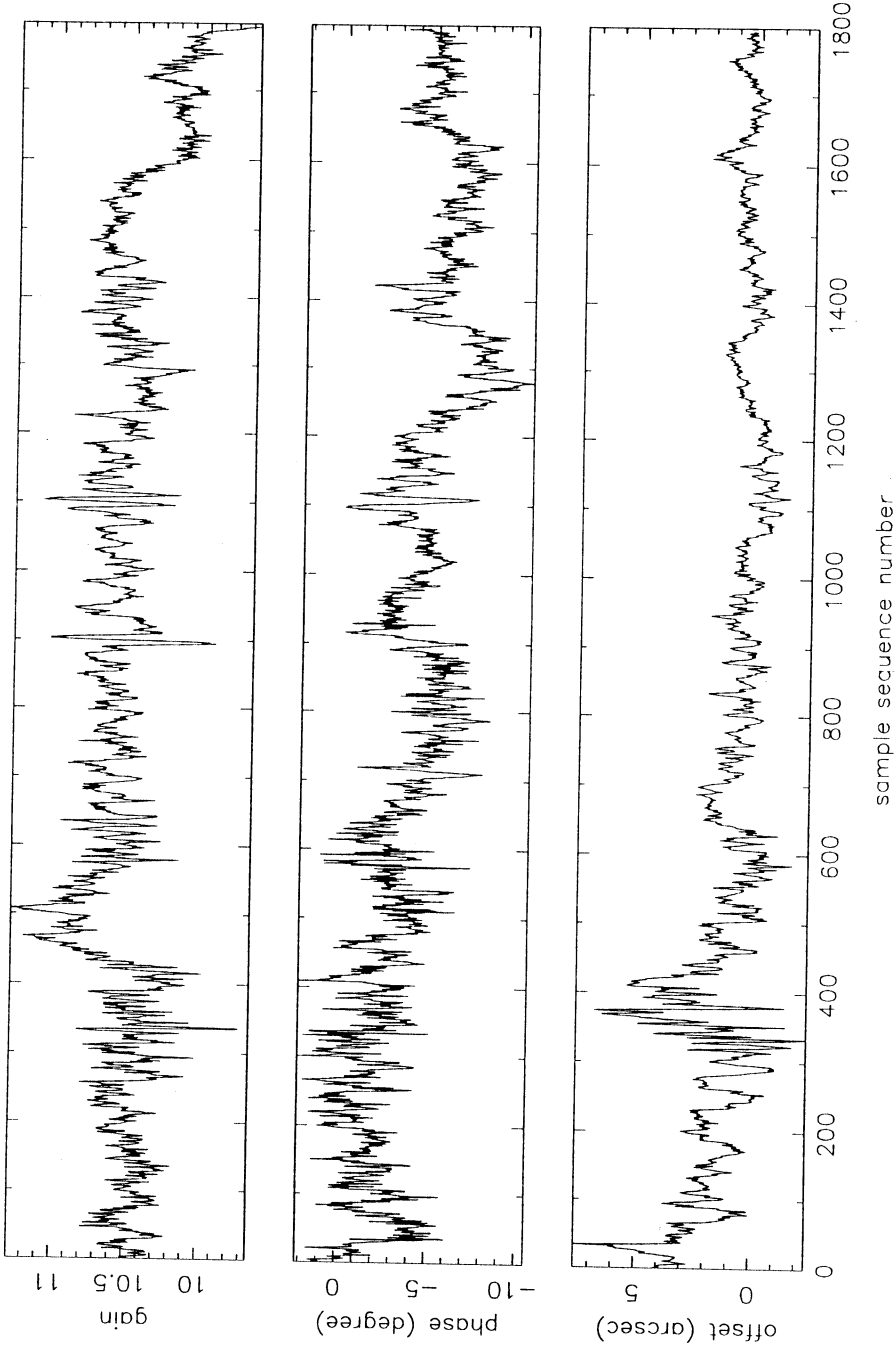


Fig. 3. Time series of the parameters $a_i(t)$ determined by the adaptive deconvolution algorithm for the observation shown in Fig. 2. The parameters correspond, from top to bottom, to a_1 , a_3 and a_2 as defined in equation (3).

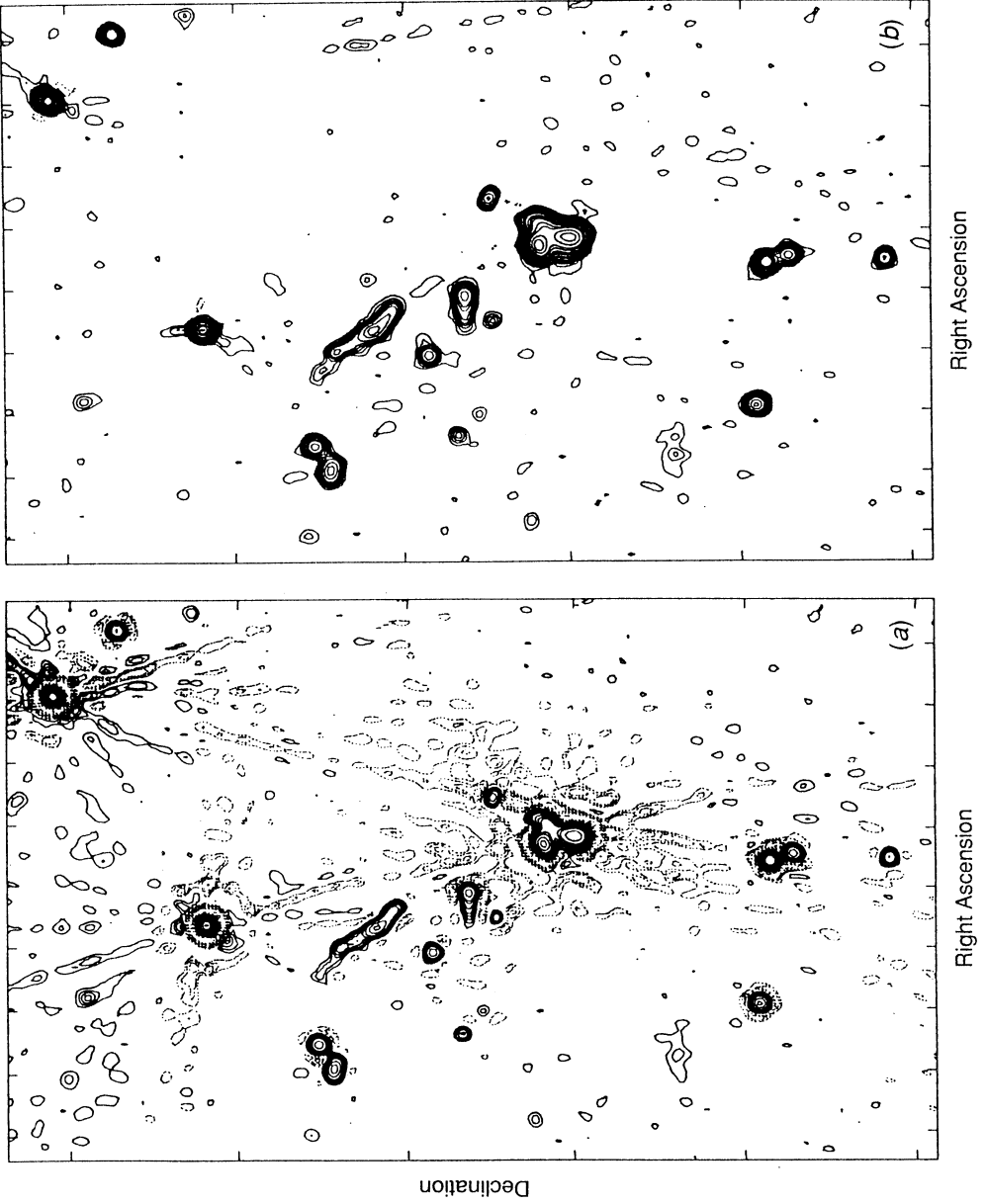


Fig. 4. Images of the cluster Abell 3266 (a) before and (b) after adaptive deconvolution. Despite the complexity of the field, the adaptive deconvolution leads to noticeable improvements (the same contour levels are used in both images). The separation between two ticks is

adjust the original data for the estimated errors. After the cycle is applied three times (only the phase term is adjusted on the first cycle) the deconvolved image shown in Fig. 2*b* results. The dynamic range in this image now approaches 1000:1, and it is clearly superior to the original image in many respects.

The field used in this test contains a strong point source. While useful for exposition, it is possible that the success of the algorithm reflects the fact that this kind of source provides an especially powerful probe of the actual PSF. To verify that we have not been misled, we have used the same algorithm to adaptively deconvolve an image of the complex radio sources in the cluster Abell 3266, as shown in Fig. 4. The method has again produced a marked improvement in the dynamic range of the image.

The effectiveness of the adaptive deconvolution method depends on the signal-to-noise ratio in the actual image. If there is insufficient signal, the least-squares fitting procedure will be dominated by the noise and the derived values of $a_i(t)$ will be unreliable. We have found in practice that the presence of a source with a flux density exceeding about 200 mJy ensures satisfactory fits. With weaker sources the fluctuations due to phase, offset and gain errors are generally invisible against the background produced by the thermal noise in the telescope receiver.

4. Discussion and Prospects

At first sight it might be surprising that the algorithm described above is successful. After all, the only data we have are strip integrals of the observed image, and yet we can determine not only the two-dimensional image but also a significant body of additional information about the performance of the telescope.

The success reflects the fact that the forms of the artifacts produced by errors in the telescope and in propagation are quite different from features seen in actual cosmic sources. By constructing an approximate *model* of the sources without including the artifacts we can amplify the errors and then fit to and remove them using an appropriate functional description of the physical origin of the artifacts. Each 24 s sample provides estimates of the physical parameters leading to artifacts, and the random error in each of these estimates can be reduced by appropriately averaging over time.

The success of the method invites extensions to models more complex than the form (6). We are presently exploring the possibility of fitting for variations in the parameters L_0 and G_0 (length and gap), which are known to depart from their actual physical values as a result of vignetting and of certain weather conditions. It may also be possible to identify the failure of one or two bays during a synthesis session, and hence to correct for their false inclusion in the ideal beam shape.

The parameters a_i derived from the deconvolution procedure have straightforward interpretations, although the physical mechanisms that lead to their variation through the course of a 12 h observation are generally unknown. A particularly interesting possibility is that fluctuations in the parameter a_3 (pointing offset) may be due to spatially variable refraction of the incoming wavefront in the atmosphere (ionosphere and troposphere). If this is the case, the accumulation of further time-series measurements of a_3 may provide useful data on the prevalence, position and amplitude of ionospheric and tropospheric fluctuations on time-scales ranging from a few seconds to several hours.

The method we have developed could be applicable in any form of tomographic imaging (e.g. X-ray, PET or ultrasound) wherein the main artifacts arise from instrumental instabilities that have a simple functional form.

Acknowledgments

We thank A. Gray for advice on this problem. The MOST is operated with partial support from the Australian Research Council and the Science Foundation for Physics.

References

- Bracewell, R. N. (1956). *Aust. J. Phys.* **9**, 198.
- Bracewell, R. N. (1978). 'The Fourier Transform and its Applications', 2nd edn (McGraw-Hill: New York).
- Christiansen, W. N., and Hogbom, J. A. (1985). 'Radiotelescopes', 2nd edn (Cambridge Univ. Press).
- Crawford, D. F. (1984). In 'Indirect Imaging' (Ed. J. A. Roberts), p. 373 (Cambridge Univ. Press).
- Gray, A. D. (1991). In 'Radio Interferometry: Theory, Techniques and Applications', IAU Colloquium 131 (Eds T. D. Cornwell and R. A. Perley), p. 202.
- Hogbom, J. A. (1974). *Astron. Astrophys. Suppl.* **15**, 417.
- Large, M. I., and Frater, R. H. (1969). *Astron. Astrophys.* **69**, 227.
- Mills, B. Y. (1981). *Proc. Astron. Soc. Aust.* **4**, 156.
- Noordam, J. E., and de Bruyn, A. G. (1982). *Nature* **299**, 597.
- Pearson, T. J., and Readhead, A. C. S. (1984). *Ann. Rev. Astron. Astrophys.* **22**, 97.
- Perley, R. A. (1979). *Astron. J.* **84**, 1443.
- Robertson, J. G. (1991). *Aust. J. Phys.* **44**, 729.
- Thompson, A. R., Moran, J. M., and Swenson, G. W. (1986). 'Interferometry and Synthesis in Radio Astronomy' (John Wiley: New York).

Manuscript received 11 August, accepted 7 November 1994